NIR/MIR Dual–Sensor Machine Vision System for Online Apple Stem–End/Calyx Recognition

X. Cheng, Y. Tao, Y. R. Chen, Y. Luo

ABSTRACT. *A near–infrared (NIR) and mid–infrared (MIR) dual–camera imaging approach for online apple stem–end/calyx detection is presented in this article. How to distinguish the stem–end/calyx from a true defect is a persistent problem in apple defect sorting systems. In a single–camera NIR approach, the stem–end/calyx of an apple is usually confused with true defects and is often mistakenly sorted. In order to solve this problem, a dual–camera NIR/MIR imaging method was developed. The MIR camera can identify only the stem–end/calyx parts of the fruit, while the NIR camera can identify both the stem–end/calyx portions and the true defects on the apple. A fast algorithm has been developed to process the NIR and MIR images. Online test results show that a 100% recognition rate for good apples and a 92% recognition rate for defective apples were achieved using this method. The dual–camera imaging system has great potential for reliable online sorting of apples for defects.*

Keywords. *Apple, Calyx, Defect inspection, Dual sensors, Dual–wavelength sensing, Imaging, Machine vision, MIR, Multi–spectrum, NIR, Stem–end.*

Apple defect inspection is an important procedure that affects the sorting or grading result in the fruit industry. Because the traditional visual apple–by–apple inspection is labor intensive and prone to human errors and variability, a machine vision system for automatic online defect inspection is needed to speed up the inspection procedure.

Near–infrared (NIR) spectroscopy has been widely used in fruit quality studies because it is quick and noninvasive. Previous research has shown that in the near–infrared range between 700 nm to 2200 nm, the reflectance from bruised areas, stem–ends, and calyxes of apples is less than from the non–bruised areas of apples. Therefore, machine vision systems equipped with near–infrared imaging sensors have been widely used in the research of apple defect inspection and quality estimation. Throop et al. (1995) developed an algorithm to identify both old and new bruises on Red Delicious apples from NIR apple images. Bollen et al. (1999) compared the methods for estimating the size of apple bruises. Paulus and Schrevens (1999) used image processing tools to quantify the average shape of randomly chosen apples. Leemans et al. (1999) exploited a color vision imaging system and a Bayesian classification method to segment apple defects. However, one of the persistent obstacles in the implementation of automatic apple defect detection is how to identify the apple stem–end/calyx. These natural parts on apples normally present similar intensity levels as true defects in a near–infrared image. As such, a computer–based automatic vision system is confused by the natural parts of an apple with true defects. This is a serious issue in apple sorting automation. Because the orientations of apples along a transportation packing line are unpredictable during the inspection process, the possibility of misclassification is unacceptably high.

To address this problem, researchers have proposed several possible solutions. Wolfe and Sandler (1985) developed an image processing algorithm to extract both long and short stems and calyxes. Miller and Delwiche (1991) proposed an orientation algorithm to recognize the surface concavities on three–dimensional information. Yang (1993) used a structured lighting system, in which controlled illumination and cameras were used to reconstruct a stereovision image of objects. Crowe and Delwiche (1996a, 1996b) designed a real–time defect detection system using structured illumination to detect stem–ends and calyxes. Most of these methods focused on detecting the natural concave shape or reconstructing the three–dimensional information of stem–ends or calyxes. In the application of a multi–lane detection system, these methods might not be suitable due to the requirement of real–time speed and accuracy.

Compared with single–spectrum inspection, which provides limited information for distinguishing the stem–ends and calyxes, multi–spectrum detection provides richer information in multiple images of different spectrum sensing results of the same object. Tao (1996, 2000), Wen and Tao (1998a, 1998b, 2000), and Tao and Wen (1999) discovered that by using a mid–infrared (MIR) camera with a spectrum range between 3 and 5 μm, bruised areas of fruit were no longer sensed and only the stem–ends and calyxes of apples

The authors are **Xuemei Cheng,** PhD Student, and **Yang Tao, ASAE Member Engineer,** Associate Professor, Department of Biological Resources Engineering, University of Maryland, College Park, Maryland; **Yud–Ren Chen, ASAE Member Engineer,** Research Leader, USDA–ARS Instrumentation and Sensing Laboratory, Beltsville, Mary–land; and **Yaguang Luo,** Research Food Technologist, USDA–ARS Produce Quality and Safety Laboratory, Beltsville, Maryland. **Corresponding author:** Yang Tao, 1426 Animal Science/Biological Resources Engineering Bldg., University of Maryland, College Park, MD 20742; phone: 301–405–1189; fax: 301–314–9023; e–mail: ytao@wam.umd.edu.

remained sensitive to the sensor. A dual–wavelength sensing method was developed and found capable of discriminating apple stem–ends and calyxes. However, in the dual–wave-length sensing system, the two image sensors must be placed at the same viewing position. In general, for typical online applications, two sensors are usually mounted at adjacent but different positions. The shift between sensing positions leads to a differences in pixel registration between the MIR and NIR images. Thus, there is a need for acquiring dual–image registration and combined algorithm for online processing.

The objective of this research was to study the feasibility of applying the dual–wavelength method and develop image processing algorithms for online apple defect inspection. In general, apples are stored in a low–temperature environment (usually 3°C to 4°C) before being inspected. This study is applied only to apples from cold storage. The algorithms, including dual–image registration, image normalization, inverse image transformation, and dual image combination, were applied to eliminate apple stem–ends and calyxes from true defects during inspection. These algorithms were studied to expand the dual–wavelength method along with the dual–image registration and synthesis strategies so that the online defect identification accuracy can be improved.

MATERIALS AND SYSTEMS
MACHINE VISION SYSTEM

The machine vision system for apple defect inspection consists of a dual–spectrum infrared sensing system and a computer–controlled image–grabbing system. A lighting chamber made by Agri–Tech, Inc., is used to provide uniform illumination for the infrared sensors. The $120 \times 100 \times 25$ cm (W $\times$ L $\times$ H) chamber is made of lattice–patterned sheet metal, and the V–shaped interior surface of the chamber is painted flat white to provide diffuse light reflection and eliminate shadows (Tao et al., 1995; Tao, 1996, 1998). Lighting is provided by ten warm–white fluorescent lamps arranged uniformly around a V–shaped surface right above the conveyor. One side of the chamber can be opened to allow camera mounting.

Two image sensors are mounted in the top center of the chamber. The near–infrared sensor utilized in the system is a Hitachi KP–MI CCD monochromatic camera with a

Corrion 700 nm interference long–pass filter and a focal length of 16 mm. The mid–infrared sensor is an Indigo uncooled thermal camera with a sensitive spectrum range from 7.5 to 13.5 microns. This camera consists of a Boeing Gen II FPA incorporating a 320×240 matrix of microbolom-eter detectors. The pixel size of the detector is 51×51 μm, and the standard focal length is 25 mm. The two infrared sensors are synchronized to obtain images at the same pace. Both near–infrared images (NIR image) and mid–infrared images (MIR image) are captured, processed, and analyzed by a host computer equipped with an imaging board (Matrix Meteor/RGB).

A roller conveyor belt is constructed to support and move apples for up to six lanes. The apples are rotating and moving when they are passing through the field of view of the image sensors. The online imaging system grabs images at a rate of 30 frame/sec, which guarantees that the entire surface of each apple will be imaged and processed. A drive controller and speed controller are coordinated with an optical encoder, providing timing signals for both online mechanical and electrical synchronization. The system configuration is shown schematically in figure 1.

Test samples for both good and defective Red Delicious apples were used to verify the effectiveness of the online processing algorithms. The properties of the test samples are listed in table 1. A total of 155 apples (19 good and 136 defective) were selected for the test. Samples were stored at about 4°C before testing. Shortly after they were taken out of the cold storage (less than 5 minutes), the samples were randomly placed on the roller conveyor.

DUAL IMAGING METHODS
DUAL–IMAGE REGISTRATION

Due to the sensor differences in the dual–wavelength sensing system, two images are not in a point–by–point correspondence. Coordination resolution differences exist between the two sensor images. The near–infrared image is 640×480, while the mid–infrared image is 320×240. Proper registration is needed to enable effective information compensation.

Schematic representation of the relationship among the NIR sensor, the MIR sensor, and the sensing objects is shown
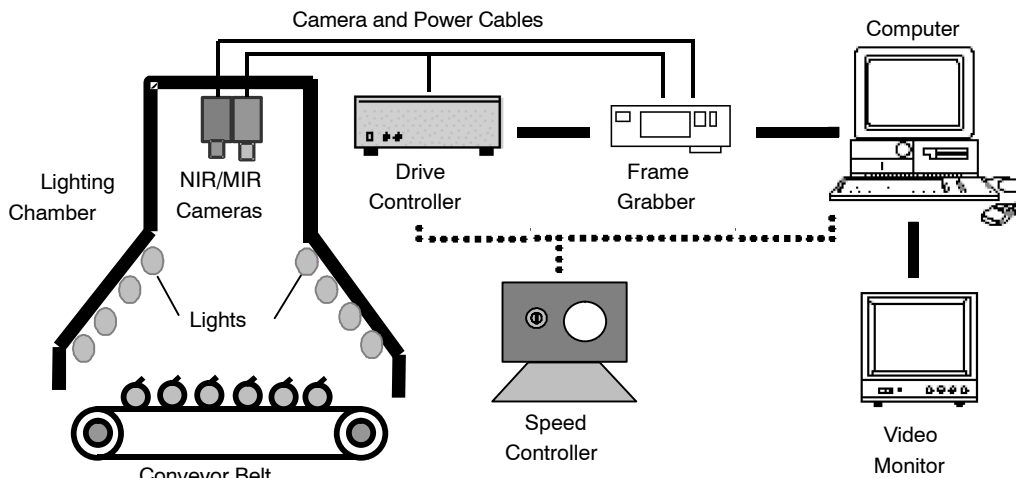

Figure 1. Schematic representation of the machine vision system for the online defect inspection.

Features	Parameters
Sample type	Red Delicious apple
Total number	155
Sample sizes	Radius: 79–81 mm and 68–70 mm
Good samples	19
Defected samples	136
Defect types	Bruise, insect holes

in figure 2. In figure 2, both sensors (camera A and camera B) are focused on object C. The horizontal distance between camera A and camera B is the camera gap and is represented by a constant (d). Let h represent the height from the lens to the conveyor belt and r represent the radius of the object. Assume that the object on the conveyor belt is spherical. Points a and b are two points on the circle that represent the limitation points of the view of camera A and camera B, and l_0 represents the horizontal distance between the object and the lens of camera A. Therefore, $l_0 + d$ is the horizontal distance from the object to camera B. The angle (θ) between points a and b represents the "blind" area between camera A and camera B. In this blind area, the object is only visible to one of the sensors. Angle θ is determined by the following equation:

$$\theta = \sin^{-1}\left(\frac{r}{\sqrt{(l_0+d)^2 + (h-r)^2}}\right)$$
$$+ \sin^{-1}\left(\frac{l_0+d}{\sqrt{(l_0+d)^2 + (h-r)^2}}\right)$$
$$- \sin^{-1}\left(\frac{r}{\sqrt{l_0^2 + (h-r)^2}}\right) - \sin^{-1}\left(\frac{l_0}{\sqrt{l_0^2 + (h-r)^2}}\right) \quad (1)$$

In our application, $h \gg d$, $h \gg r$, $h \gg l_0$, and θ approximately equals zero, which means the blind area between the dual sensors can be ignored. Both sensors, NIR and MIR, cover the same sensing range on the object.

Two–dimensional (2–D) image–coordinate transformation is necessary to map objects in the original MIR image (OMI) to those in the original NIR image (ONI). The transformation is global since it is applied to the entire image. Suppose pixel (x, y) in the OMI corresponds to pixel (u, v) in ONI, then:

$$\begin{bmatrix} x \\ y \end{bmatrix} = \Phi \bullet \begin{bmatrix} u \\ v \\ 1 \end{bmatrix} = \begin{bmatrix} a & b & x_0 \\ c & d & y_0 \end{bmatrix} \begin{bmatrix} u \\ v \\ 1 \end{bmatrix} \quad (2)$$

where Φ is the 2×3 transformation matrix. Elements a, b, c, and d in Φ are the factors related to the possible scaling and rotation of the two coordinate systems. Elements x_0 and y_0 represent the displacements in the x– and y–axes, respectively. Matrix Φ can be solved by picking at least six points in the mid–infrared image plane, and obtaining at least six sets of x, y, u, and v values for equation 2.

The different focal lengths of the two sensors in the system cause resolution differences (NIR image resolution is 1.09 mm/pixel; MIR image resolution is 1.27 mm/pixel) between the original near–infrared and mid–infrared images. The same objects appear different sizes in the mid–infrared and the near–infrared images. In our system, the image size of an object in a mid–infrared image is smaller than that in a near–infrared image. A bilinear interpolation method is used to rescale the mid–infrared image. In this way, the system resolution is unified as 1.09 mm/pixel. Suppose the scaling factors in the x and y directions are d_x and d_y, respectively, as shown in figure 3. Bilinear interpolation takes the weighted average of a 2×2 pixel neighborhood as the assigned value to evaluate the interpolated pixel. Weights are determined by measuring the distance from the interpolated pixel to its nearest four surrounding pixels. The value of the interpolated pixel (P) in figure 3 can be evaluated as follows:

$$p_{12} = d_x p_1 + (1-d_x)p_2$$

$$p_{34} = d_x p_3 + (1-d_x)p_4$$

$$p = d_y p_{12} + (1-d_y)p_{34}$$
$$= d_x d_y p_1 + (1-d_x)d_y p_2 + d_x(1-d_y)p_3$$
$$+ (1-d_x)(1-d_y)p_4 \quad (3)$$

where

p_1, p_2, p_3, p_4 = the pixel values from a 2×2 pixel neighborhood of the interpolated pixel P

p = pixel value of P

p_{12} and p_{34} = intermediate pixel values used to derive the value of p.
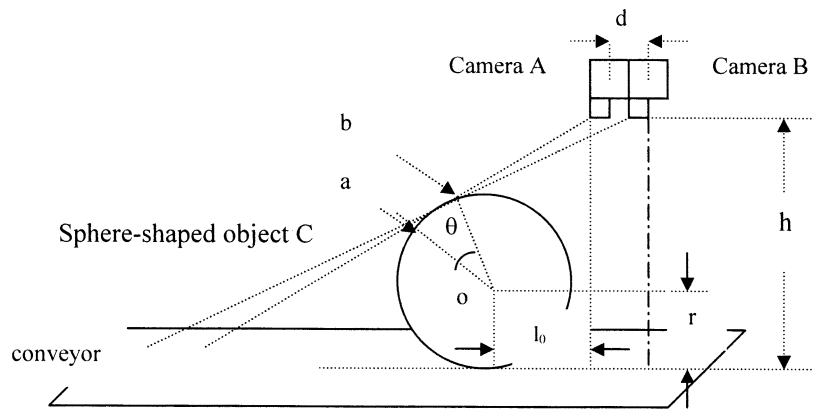

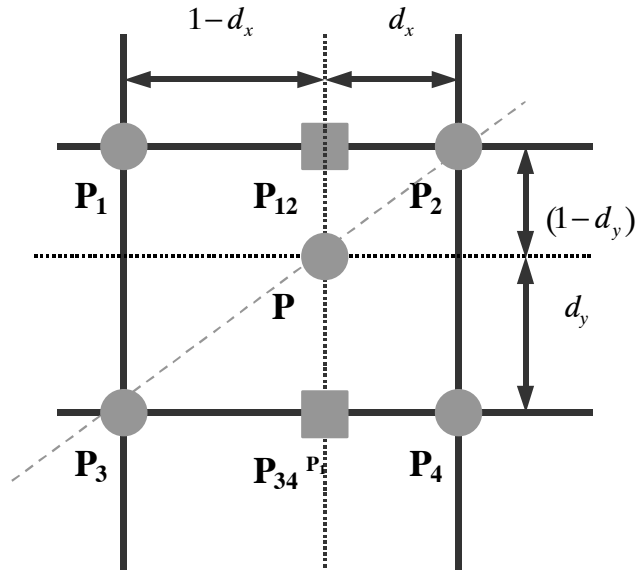**Figure 2. Schematic representation of the relationship among the sensing objects and the NIR/MIR sensors.**
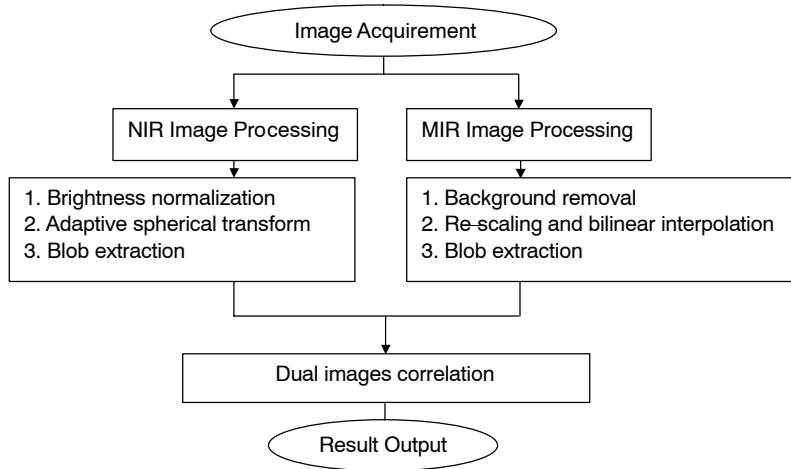
Figure 3. Schematic representation of binary interpolation.

Figure 4. Flowchart of the online image processing procedure.

DUAL–IMAGE PROCESSING

Figure 4 shows a flowchart of the dual–image preprocessing and combination schemes applied in this study. Separated processing methods were applied to the dual sensor images, and the combination results were evaluated.

NIR Image Normalization

In the near–infrared spectrum from 700 to 1000 nm, a dark–colored fruit has a lower light reflectance than a bright–colored fruit. Different brightness levels cause detection errors, especially for bright–colored defective apples and dark–colored good apples. To avoid these kinds of errors, a normalization operation is applied to the original NIR image (ONI). The details of the method can be found in Wen and Tao (1998a, 1998b). The normalized NIR image (NNI) can be obtained from ONI by eliminating the effect of the brightness variations in ONI:

$$NNI(x,y) = c_0 \frac{ONI(x,y)}{I_{\max}(x,y)} \qquad (4)$$

where
$I_{\max}(x, y) = \max[ONI(x, y)]$ for all (x, y)
c_0 = constant equal to 255 in this application.
$I_{\max}$ is generated by a recursive calculation represented by the following formulation:

$$I_{\max}(x,y)_k = \max\{I_{\max}(x-x',y-y')_{k-1} + B(x',y')|(x-x',y-y') \in D_I ; (x,y) \in D_B \qquad (5)$$

$$I_{\max}(x,y)_0 = ONI(x,y); k = 1,2,3... \qquad (6)$$

where
B = all–zero 3×3 mask matrix
D_I = domain of $I_{\max}$
D_B = domain of B.

Adaptive Spherical Transform for NIR Image

Apples are considered to have substantially spherical shapes. The curved apple surface causes inconsistent reflection of the light. As a result, in an NIR image, the intensity distribution on sensed apples is not uniform. The pixels
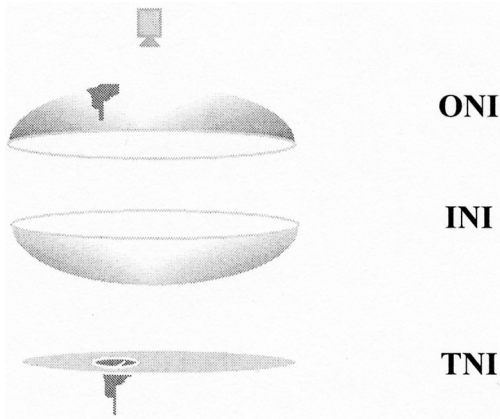
Figure 5. Schematic representation of the principle of spherical transformation.

Figure 6. Spherical transform curves for two different–sized objects.

around the boundary of the apple appear at a much lower intensity than the central pixels. The defective portions of apples also appear at a low intensity in the NIR image, and the intensity levels of the two kinds of pixels are comparable.

An effective method, called the adaptive spherical transform method, is used to distinguish them. A detailed description of this method can be found in Tao (1996) and Tao and Wen (1999). The idea of this method is to transform the edges of spherical objects to an intensity level near the intensity of the center, and thus to generate a plane object image with uniform intensity without losing defect information. The basic principle can be represented as shown in figure 5. Three images are involved in the transformation process: a normalized near–infrared image (I_{NN}), an inversed image (I_{NN}^{-1}), and a synthesized image. The inversed image (INI) is a mirror image of NNI with the same shape and image size but without any defects. INI is generated by the following equation:

$$INI(x, y) =$$
$$c_0\{1 - R_N(s;(x, y))\};(x, y) \subset NOI(x, y), s \subset S_d\} \quad (7)$$

where
  s = size of the apples
  S_d = subset of size variation in pixels.
$R_N[s; (x, y)] = OOI[s; (x, y)] / I_{max}[s; (x, y)]$ is the reflection correction function. The light reflectance on the curved surface differs from point to point. The inversed image INI can be considered as a group of transformation curves varied by different sizes of the objects. The transformation curves of two different–sized objects are shown in figure 6. The TNI is obtained by combining NNI and INI:

$$TNI(x, y) = NNI(x, y) + INI(x, y), (x, y) \subset s_i \quad (8)$$

where s_i represents the pixels within the range of interest in NNI.

Global Threshold on MIR Image

The mid–infrared sensor is sensitive to the temperature differences on the objects within its field of view. Low–temperature objects present less intensity in the mid–infrared image than high–temperature objects. According to the different material characteristics and concave shape on both stem–ends and ca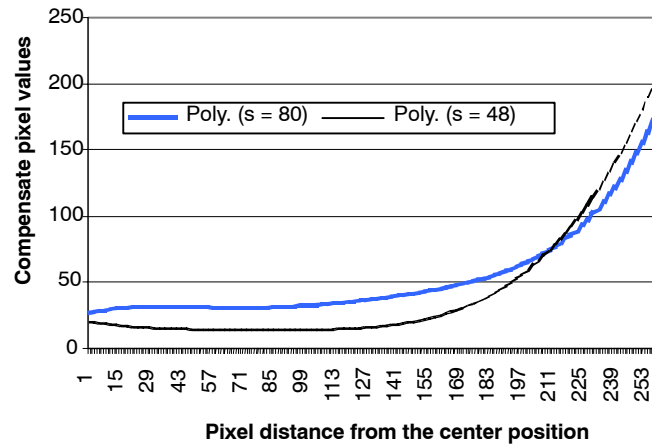lyxes of apples, the temperature in these areas of the apple is lower than in other parts of the apple surface after being refrigerated. As a result, stem–ends or calyxes appear different from the other part of the apple by presenting a lower intensity level in the MIR image. On the contrary, defects show the same intensity levels as the non–defective parts of apples.

To extract the stem–ends and calyxes from the original MIR apple images, the background is removed and only the object of interest is considered. A global threshold is used for the original MIR image to obtain the MI image as:

$$MI(x, y) = \begin{cases} OMI(x, y) & OMI(x, y) < T_1 \\ 0 & others \end{cases} \quad (9)$$

where T_1 is the global threshold value.

Blob Analysis on NIR and MIR

Blob analysis is performed on the TNI and MI images separately to classify the pixels into different regions (or blobs). To apply blob analysis, two steps are needed: blob identification and blob labeling. Blob identification is used to categorize pixels into groups according to the similarity of certain features. Blob labeling is used to segment the identified pixels into different blobs according to their spatial positions.

Pixels with similar features are classified into the same group. Feature vectors are used to describe those features. For instance, let x_k be the feature vector for pixel k. Mathematically, x_k is represented as $x_k = [x_{k1}, x_{k2},..., x_{km}]^T$. Similarly, x_j is the feature vector for pixel j, and can be expressed as $x_j = [x_{j1}, x_{j2},..., x_{jm}]^T$. To judge the similarity of the two pixels, the Euclidean distance between two feature vectors (E_{jk}) is calculated as:

$$E_{jk} =$$
$$\sqrt{(x_{j1} - x_{k1})^2 + (x_{j2} - x_{k2})^2 + ... + (x_{jm} - x_{km})^2} \quad (10)$$

If a threshold feature vector x_0 is given, then all pixels in the image can be separated into two groups.

In both TNI and MI, the feature of a pixel is simply equal to the gray level of the pixel. For TNI, the pixels are segmented into non–defective and defective (including stem–ends and calyxes) groups. In MI, pixels are also segmented into two groups: stem–ends/calyxes and blobs, where the blob represents the other portion of the apple. For

a given feature vector x_0, the segmented image is called the blob identification image (BII), which can be obtained by:

$$BII(x_k, y_k) = \begin{cases} 1 & E_{k0} < E_{th} \\ 0 & others \end{cases} \quad (11)$$

Here, E_{th} is a threshold value for Euclidean distance.

Blob labeling is used to identify the connected component in BII. The algorithm seeks to identify connected groups of pixels in BII that all have the same binary value 1 by scanning the entire image from top to bottom and from left to right. Let $r(x, y)$ represents the blob–labeling image. When the BII(x, y) = 1, the process of the algorithm used to determine the $r(x, y)$ can be described as follows:

$$r_{ini}(x, y) = 0;$$

$$r(x, y) = \quad (12)$$

$$\begin{cases} 0 & BII(x-1, y) = BII(x, y-1) = 0; \\ r(x-1, y) = 1 & BII(x-1, y) = 1 \,\&\, BII(x, y-1) = 0; \\ r(x, y-1) = 1 & BII(x-1, y) = 0 \,\&\, BII(x, y-1) = 1; \\ r(x-1, y) = r(x, y-1) = 1 & BII(x-1, y) = 1 \,\&\, BII(x, y-1) = 1; \end{cases}$$

After performing the two steps of blob analysis to TNI and MI, blob–extracted NIR images (BNI) and blob–extracted MIR images (BMI) are obtained.

DUAL–IMAGE SYNTHESIS

The BNI and BMI images are compared to remove stem–ends and calyxes from true defects in the results. The combination of BNI and BMI is used to decide which blob extracted in BNI represents the stem–end or calyx. In the final combined image (CI), the blobs that represent the stem–ends or calyxes are eliminated, and only the blobs of true defects remain. CI is generated by a recursive calculation:

$$CI_k(x, y) = \begin{cases} 0 & if\ BNI(x, y) = k\ and\ BMI(x, y) \neq 0 \\ BNI(x, y) & others \end{cases} \quad (13)$$

$$CI_{k+1}(x, y) = \begin{cases} 0 & if\ CI_k(x, y) = k; \\ CI_k(x, y) & others \end{cases} \quad (14)$$

where $k = 1,..., N$ represents the N number of blobs in BNI.

RESULTS AND DISCUSSION

A series of the intermediate images and the final image are presented in figure 7. Figure 7a represents the original NIR image output from the NIR sensor. The apple in the lower right is a non–bruised apple, which was used as the control. Each of the other three apples has at least one defect (the apple in the upper left has two defects). Note that, except for the apple in the upper left, the original near–infrared image shows the stem–end of the apple. The brightness levels of the apples are not uniform. The maximum gray level in the original near–infrared image is typically around 190, and the minimum gray level is 25. The dynamic range of the image is 165.

The normalized NIR image is shown in figure 7c. Notice that the brightness levels of the apples were adjusted to be the
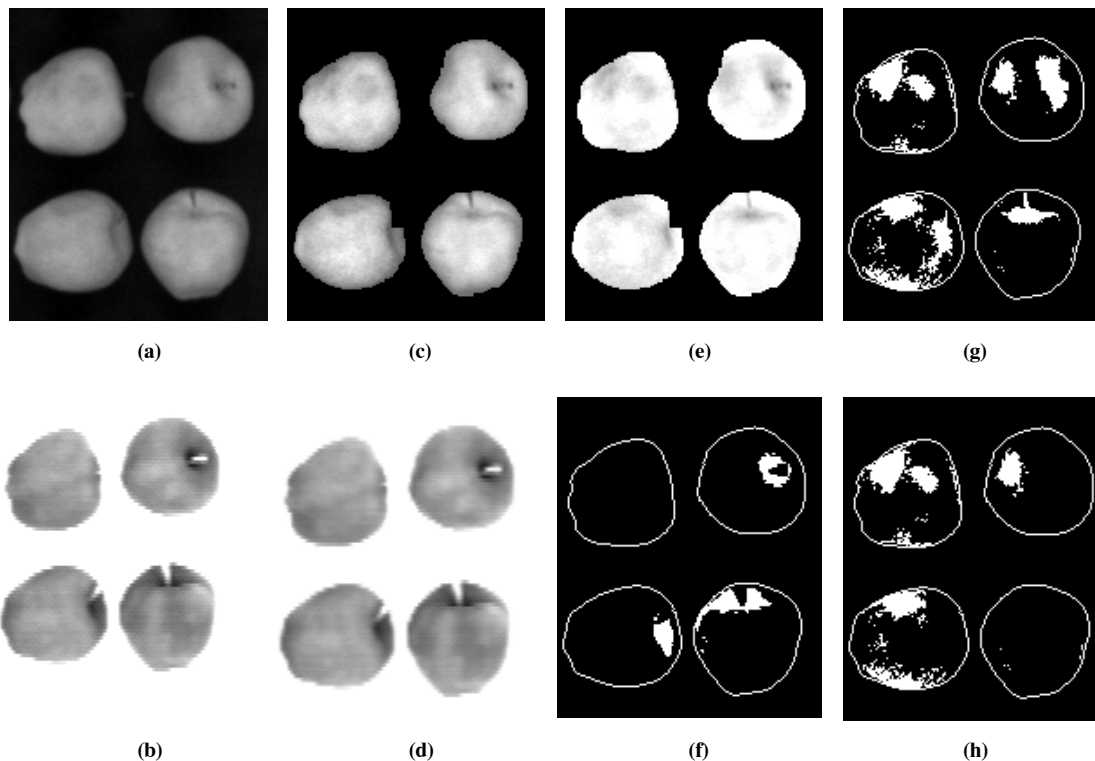

Figure 7. An example result of the dual–sensor NIR/MIR algorithm: (a) the original NIR image, (b) background–removed MIR image, (c) normalized NIR image, (d) resized MIR image, (e) adaptive–transformed NIR image, (f) blob–extracted MIR image, (g) blob–extracted NIR image, and (h) final NIR/MIR combination image.

same. The maximum gray level of the image became 255. Thus, the dynamic range of image was widened to the maximum. However, the boundaries around the apples show obviously lower gray levels compared with the center parts.

The adaptive spherical transformation method via equations 7 and 8 was used to address this problem. As shown in figure 7e, the gray levels around the boundary areas of the apples were boosted to be the same as the center areas. The non–bruised areas of the apples are now in the same gray–level plane, while the gray levels in the defective areas remain unchanged. It becomes much easier to apply the blob feature extraction analysis to the transformed NIR image than to the raw NIR image. The extracted blobs containing true defects, stem–ends, and noises are shown in figure 7g. Noises are usually small blobs, ranging from one to three pixels in area. These small blobs can be eliminated by morphological operations.

Small defects that are three or four pixels in area $(3\sim4 \text{ mm}^2)$ are sometimes confused with noises. Applying the morphological operations to eliminate the noises requires the proper threshold value to measure the blob size of the noise. If the recognition accuracy of small defects is important, then the threshold value should be small, such as two pixels. If a good apple classification rate is crucial, then the threshold value should be larger, such as four pixels. A good tradeoff value should be determined according to different applications.

For the mid–infrared thermal sensor, the sensed image is different from the near–infrared one. Figure 7b shows the image of the same four apples sensed by the thermal camera. The background information removed is shown in figure 7b. It can be observed that the sizes of the objects in the image are smaller compared with those in the ONI image (fig. 7a). The registration of the two images involves the operations of coordinate transformation and linear interpolation. The result is shown in figure 7d, where the objects are of the same sizes as those in the NIR images. In the MIR images, the gray levels of stem–ends are lower than those of the other areas of the apples. The defective areas become "invisible" to the sensor. Blob analysis of the MIR image results in the recognition of only the stem–ends of the apples, as shown in figure 7f.

Based on the information in figures 7f and 7g, the images are combined, compared, and compensated to produce the final image shown in figure 7h. Only true defects are obtained in the result.

During the testing, a total of 36 stem–ends and 48 calyxes were sensed within the field of view for each camera. The final classification rates for the stem–ends and calyxes are shown in figure 8. Recognition rates of about 94% for stem–ends and 92% for calyxes were achieved on the test samples.

All of the 19 good apples were classified as good during the test. A classification accuracy of 100% was therefore obtained for good apples. A classification accuracy of 92% was achieved for defective apples. The recognition rates for both good apples and defective apples show the feasibility and efficiency of the dual–sensor method. The misclassifications usually happened in two situations: when the stem–end or calyx appeared near the edge of the observed apple surface, or when small defects appeared very near the stem–ends or calyxes. The first situation can be improved by
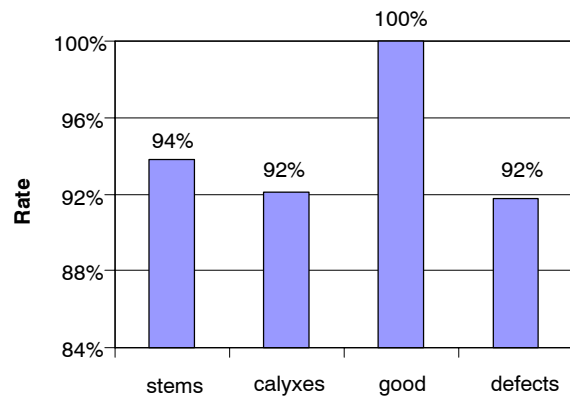

Figure 8. Test result of sample recognition rates for online dual NIR/MIR sensing algorithm.

adjusting the threshold values in the imaging algorithms, while the second situation can be improved by performing the morphological operations.

Another factor that might affect the inspection results is the temperature distribution on the surface of the test samples. The thermal camera is sensitive to temperature changes above $0.1°C$. It is impossible to implement absolutely uniform temperature distribution during the online tests. Some apple samples have non–uniform temperature distribution on their surfaces. As a result, non–uniform changes in gray levels were observed in the MIR images. Fortunately, these non–uniform distributions of gray levels were not significant, and proper selection of the global threshold in the MIR algorithm would minimize their influence.

CONCLUSIONS

An online dual–sensor NIR/MIR imaging method has been proposed and presented in this article. The sensing effects of the dual–spectrum system were examined, and a classification accuracy of more than 92% was achieved for online apple defect recognition. Using the 700–750 nm wavelength sensor, both defects and stem–ends on the apple were detected. The thermal sensor with a spectrum of 7.5 to 12.5 microns was demonstrated to be effective in identifying the stem–ends and calyxes on the apples.

The statistical results on the performance of the algorithms show the feasibility of the dual–sensing methodology. The 100% recognition rate for good apples shows that the system is sensitive to type–I errors. The test results also show that the proposed method of image registration and dual–image combination reduces the possible misclassification rate of stem–ends and calyxes to 6% and 8%, respectively. The methodology and algorithms can be considered an extension of the inspection strategy and be used for other fruits or similar objects.

REFERENCES

Bollen, A. F., H. X. Nguyen, and B. T. D. Rue. 1999. Comparison of methods for estimating the bruise volume of apples. *J. Agric. Eng. Research* 74(4): 325–330.

Crowe, T. G., and M. J. Delwiche. 1996a. Real–time defect detection in fruit — Part I: Design concepts and development of prototype hardware. *Trans. ASAE* 39(6): 2299–2308.

_____. 1996b. Real–time defect detection in fruit — Part II: An algorithm and performance of a prototype system. *Trans. ASAE* 39(6): 2309–2317.

Leemans, V., H. Magein, and M. F. Destain. 1999. Defect segmentation on 'Jonagold' apples using colour vision and a Bayesian classification method. *Computers and Electronics in Agric.* 23(1): 43–53.

Miller, B. K., and M. J. Delwiche. 1991. Peach defect detection with machine vision. *Trans. ASAE* 34(6): 2588–2597.

Paulus, I., and E. Schrevens. 1999. Shape characterization of new apple cultivars by Fourier expansion of digitized images. *J. Agric. Eng. Research* 72(2): 113–118.

Tao, Y. 1996. Spherical transform of fruit images for on–line defect extraction of mass objects. *Opt. Eng*. 35(2): 334–350.

_____. 1998. Closed–loop search method for on–line automatic calibrations of multi–camera inspection systems. *Trans. ASAE* 41(5): 1549–1555.

_____. 2000. Photonics in fruit and vegetable quality assessment. In *Critical Review of Optics in Agriculture 1990–2000* (vol. CR80): 65–100. Bellingham, Wash.: SPIE.

Tao, Y., and Z. Wen. 1999. An adaptive spherical image transform for high–speed fruit defect detection. *Trans. ASAE* 42(1): 241–246.

Tao, Y., L. Chance, and B. Liu. 1995. Full–scale machine vision sorting system design – Factors and considerations. In *Food Processing Automation*, vol. III: 14–22. St. Joseph, Mich.: ASAE.

Throop, J. A., D. J. Aneshansley, and B. L. Upchurch. 1995. An image processing algorithm to find new and old bruises. *Applied Eng. in Agric*. 11(5): 751–757.

Wen, Z., and Y. Tao. 1998a. Method of dual–camera NIR/MIR image for fruit sorting. ASAE Paper No. 983043. St. Joseph, Mich.: ASAE.

_____. 1998b. Dual–wavelength imaging for online identification of stem ends and calyxes. *Proc. SPIE* 3460: 249–253.

_____. 2000. Dual–camera NIR/MIR imaging for stem–end/calyx identification in apple defect sorting. *Trans. ASAE* 43(2): 449–452.

Wolfe, R. R., and W. E. Sandler. 1985. An algorithm for stem detection using digital image analysis. *Trans. ASAE* 28(2): 641–644.

Yang, Q. 1993. Finding stalk and calyx of apples using structured lighting. *Computers and Electronics in Agric*. 8(1): 31–42.